

The Development and Structure of an Oceanic Squall-Line System during the South China Sea Monsoon Experiment

JIAN-JIAN WANG

*Goddard Center for Earth Science and Technology, University of Maryland, Baltimore County, and
Mesoscale Atmospheric Processes Branch, NASA Goddard Space Flight Center, Greenbelt, Maryland*

LAWRENCE D. CAREY

Department of Atmospheric Sciences, Texas A&M University, College Station, Texas

(Manuscript received 15 December 2003, in final form 29 October 2004)

ABSTRACT

A primary goal of the South China Sea Monsoon Experiment (SCSMEX), a major field campaign of the Tropical Rainfall Measuring Mission (TRMM), is to define the initiation, structure, evolution, and dynamics of precipitation processes associated with the onset of the South China Sea (SCS) summer monsoon. In this study, dual-Doppler and dual-polarimetric radar analysis techniques are used to investigate the development and structure of a squall-line system observed on 24 May 1998. The focus is the linkage between the airflow and the microphysical fields through the system.

The squall-line system, including three distinct lines, persisted from 1200 UTC 24 May to the following day. A detailed study was performed on the structure of the second and most intense line, lasting for over 10 h. Compared to tropical squall lines observed in other regions, this narrow squall-line system had some interesting features including 1) maximum reflectivity as high as 55 dBZ; 2) relatively little stratiform rainfall that preceded instead of trailed the convective line; and 3) a broad vertical velocity maximum in the rear part of the system, rather than a narrow ribbon of vertical velocity maximum near the leading edge.

Polarimetric radar-inferred microphysical (e.g., hydrometeor type, amount, and size) and rainfall properties are placed in the context of the mesoscale morphology and dual-Doppler-derived kinematics for this squall-line system. A comparison is made between results from this study for SCSMEX and the previous studies for the TRMM Large-Scale Biosphere–Atmosphere experiment (LBA). It was found that precipitation over the SCS monsoon region during the summer monsoon onset was similar to the precipitation over the Amazon monsoon region during the westerly regime of the TRMM–LBA, which has previously been found to be closer to typical conditions over tropical oceans. Both of these cases showed lower rain rates and rainwater contents, smaller raindrops, and significantly lower ice water contents between 5 and 8 km than the precipitation over the Amazon during the easterly regime of the TRMM–LBA with more tropical continental characteristics.

1. Introduction

The evolution and structure of convection in the Tropics are of considerable interest because of their impact on heat, moisture, and momentum fluxes. Characterization of the vertical structure of tropical convection is a major objective of the Tropical Rainfall Measuring Mission (TRMM) launched by the National Aeronautics and Space Administration (NASA; Simpson 1988). To support TRMM, a series of field campaigns were conducted in various tropical locations in

order to provide detailed information on tropical convection. The South China Sea Monsoon Experiment (SCSMEX), conducted in the South China Sea (SCS) and surrounding area in 1998, aimed at a better understanding of the key physical processes for the onset, maintenance, and variability of the monsoon over Southeast Asia and southern China leading to improved monsoon predictions (Lau et al. 2000; Tao et al. 2003). The SCSMEX also served as one of the TRMM experiments that was designed to study the precipitation and kinematic structures of mesoscale convection in an oceanic environment.

The east Asian monsoon is an important component of the regional and global climate. The precipitation processes associated with the summer monsoon play an

Corresponding author address: Dr. Jian-Jian Wang, Mesoscale Atmospheric Processes Branch, NASA Goddard Space Flight Center, Greenbelt, MD 20771.
E-mail: jjwang@agnes.gsfc.nasa.gov

important role in the agriculture and people's daily life of the Southeast and east Asian countries. For instance, the quasi-stationary rainbelt, so called mei-yu in China and Baiu in Japan, may cause disastrous floods in the region when excessive rainfall occurs. Although the east Asian summer monsoon attracts more attention when it affects the land area to the north during June–August, the onset of the east Asian summer monsoon starts over the ocean to the south in the SCS region in May (Tao and Chen 1987). In 1998, the SCS summer monsoon onset included three steps (Ding and Liu 2001; Lau et al. 2002): 1) the low-level southwesterly winds from the Tropics prevailed in the northern SCS on 15 May; 2) the southwesterly monsoon flow at low levels spread to the whole SCS by 20 May; and 3) the upper-level northeasterly winds were established over the SCS region by 23–24 May. There were basically two types of precipitation processes over the northern SCS during the 10-day monsoon onset period (Wang 2004). The first type was the well-organized cloud system associated with an extratropical cyclone from northwestern China. The interaction between the tropical monsoon flow and the frontal circulation played an important role in the organization and structure of the mesoscale convection. The second type was related to a mesoscale vortex that developed in the northern Indochina peninsula and southern China. Periodically, when a mesoscale vortex drifted eastward along with the southern branch of westerlies around the Tibetan Plateau, convection erupted in the northern SCS to the east of the vortex. The associated rainfall was relatively localized but intense. Waterspouts and severe squall lines were observed in the northern SCS when influenced by the tropical mesoscale vortex from the west. To document the organization and structure of monsoon convection during the early onset stage, Wang (2004) performed a mesoscale analysis of the precipitation systems on 15 May, which were good examples of the first type of the precipitation process. In this study, we will focus on the evolution and structure of a squall-line system observed on 24 May, which was representative of the second type of the precipitation process.

The general characteristics of tropical squall lines were obtained initially by analyzing aircraft and sounding datasets from the Line Islands Experiment (Zipser 1969) and the Global Atmospheric Research Program (GARP) Atlantic Tropical Experiment (GATE; Houze 1977). Using dual-Doppler radar analysis, Chong et al. (1987) documented the detailed kinematic fields of an African squall line. Since then, the dual-Doppler radar technique has been used as an essential ingredient for studies of precipitation and kinematic structure of tropical and midlatitude squall lines (e.g., Roux 1988;

Biggerstaff and Houze 1991; Jorgensen et al. 1997). It was found that the structures of tropical and midlatitude squall lines are very similar. Their relatively simple structure usually consists of a convective region at the leading edge, a stratiform region to the rear, and a weak reflectivity transition zone. In the convective part, updrafts are generated by the convectively driven descending air colliding with the incoming moist environmental air near the leading edge. The updraft usually tilts rearward and extends at upper levels in the stratiform region. In the stratiform region, a weak updraft is often observed above the melting layer with a weak downdraft beneath (Houze 1993). The fast-moving ($>7 \text{ m s}^{-1}$; Barnes and Sieckman 1984) squall lines generally propagate near the speed of the low-level jet maximum when the convective line is oriented roughly perpendicular to the low-level wind shear (Keenan and Carbone 1992). The convective and stratiform rains of squall lines have also been numerically simulated with considerable success (Fovell and Ogura 1988, 1989; Tao and Simpson 1989; Trier et al. 1996, 1997; Lewis et al. 1998). Nevertheless, it is well recognized that considerable differences in the detailed rainfall and kinematic structures exist in tropical convection in different areas (Zipser 1977; Keenan and Carbone 1992; LeMone et al. 1998). Differences in the vertical distribution of precipitation and latent heating in mesoscale convection also result in a very different response by the large-scale circulation (Raymond 1994).

Prior to SCSMEX, no systematic study of linear convection over the SCS monsoon region had been conducted, because the traditional observational network was inadequate over the ocean. Work related to the monsoonal convection in the SCS include the studies on subtropical squall lines observed during the Taiwan Area Mesoscale Experiment (TAMEX). Wang et al. (1990) found that the structural features of the squall lines to the northwest of Taiwan were similar to those for a fast-moving tropical squall line. Front-to-rear flow prevailed at all levels in the front side and was accompanied by shallow rear-to-front flow on the back. Convective downdrafts occurred behind the main cells. A squall line located near the east coast (leeside) of Taiwan was also investigated by Jorgensen et al. (1991) using airborne Doppler radar. However, that squall line occurred in mid-June in the late mei-yu season. The evolution and structure of the system was also strongly influenced by the steep island topography of Taiwan.

More recently, several studies of monsoon convection in other tropical and subtropical regions focused on both the vertical structure of hydrometeors and the kinematic quantities (e.g., Carey and Rutledge 2000; Cifelli et al. 2002). Those results provided important

information on the corresponding location of latent heat release, which is a driving force in the global circulation. The tropical island convection studied by Carey and Rutledge (2000) was characterized by strong midlevel updrafts, vertically extensive differential reflectivity columns, and hail/frozen drop zones. During the TRMM Large-Scale Biosphere–Atmosphere experiment (LBA, January–February 1999), Cifelli et al. (2002) found that there was an active mixed phase zone in the easterly regime that was largely absent in the westerly regime. The thermodynamic, wind, aerosol, and resulting convective systems over the southwestern Amazon during the westerly regime were closer to typical conditions over tropical oceans while conditions during the easterly regime were more characteristic of archetypical tropical continental regimes (Halverson et al. 2002).

The main objective of the mesoscale program of the SCSMEX is to define the initiation, structure, evolution, and dynamics of precipitation systems associated with the onset and mature phase of the SCS summer monsoon. In this study, we will perform a detailed analysis of the evolution and structure of a squall-line system that was observed for the first time in the SCS region during the summer monsoon season. Our focus is to investigate the linkage between the flow through the convective system and the microphysical fields retrieved from the polarimetric data. In section 2, the dual-Doppler and polarimetric radar data analysis techniques are briefly described, as well as the analysis methods used to assess the mesoscale structure of the convection. Section 3 presents an overview of the synoptic-scale conditions on 24 May. In section 4, the formation and evolution of the squall-line system observed on 24 May are reviewed. The rainfall and kinematic structures derived from dual-Doppler radar analysis are presented in detail in section 5. The rainfall and hydrometeor characteristics of the squall lines are also analyzed in section 6 using the polarimetric radar data. Some statistical results from the case study of 24 May are performed in section 7. Finally, a summary is given in section 8.

2. Data and analysis

The field phase of SCSMEX was from 1 May to 30 June 1998 including two intensive observation periods (IOPs): 5–25 May and 5–25 June. A variety of instrumentation was deployed in the experiment including C-band Doppler and polarimetric radars forming a dual-Doppler radar network (Fig. 1), enhanced sounding network, and surface meteorological and rainfall observations. The primary data used in this study are radar data including both the conventional and polarimetric variables. During SCSMEX, the National Oceanic and Atmospheric Administration (NOAA) Tropical Oceans Global Atmosphere (TOGA) radar was installed on the People's Republic of China *Shiyan-3* research vessel (about 20.4°N, 116.8°E) and operated continuously during the two IOPs, and the Bureau of Meteorology Research Centre (BMRC, Australia) polarimetric C-POL radar was installed at Dongsha Island (20.7°N, 116.7°E) and operated on a 24-h basis (with several short breaks) throughout May and June 1998. The additional sources of information used in this study for larger-scale background also include synoptic reanalysis charts from the National Centers for Environmental Prediction (NCEP), satellite imagery, and a sounding network.

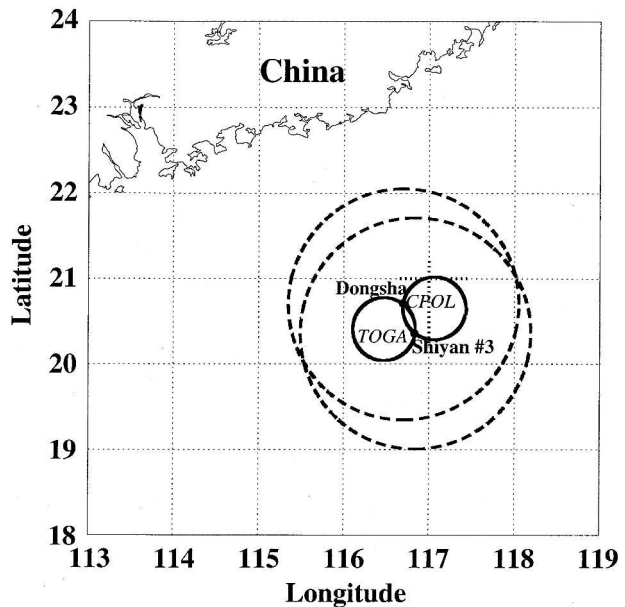


FIG. 1. Dual-Doppler radar network over the SCS during SCSMEX. The big dashed circles indicate the radar-observing domain, while the small solid circles show the dual-Doppler radar analysis regime.

anic and Atmospheric Administration (NOAA) Tropical Oceans Global Atmosphere (TOGA) radar was installed on the People's Republic of China *Shiyan-3* research vessel (about 20.4°N, 116.8°E) and operated continuously during the two IOPs, and the Bureau of Meteorology Research Centre (BMRC, Australia) polarimetric C-POL radar was installed at Dongsha Island (20.7°N, 116.7°E) and operated on a 24-h basis (with several short breaks) throughout May and June 1998. The additional sources of information used in this study for larger-scale background also include synoptic reanalysis charts from the National Centers for Environmental Prediction (NCEP), satellite imagery, and a sounding network.

A more detailed description of the issues related to radar data quality control and process was given by Wang (2004). In brief, due to a misaligned bandpass filter on the TOGA radar, the reflectivity (Z) measured by the TOGA was significantly biased. Therefore, only the reflectivity data collected from C-POL will be used in this study. The quality controlled radial velocity data from both TOGA and C-POL were unfolded and interpolated to a Cartesian grid using the National Center for Atmospheric Research (NCAR) REORDER software (Mohr et al. 1986). With a 40–45-km-long baseline, a 30° intersection angle between beams of the radar, which is required for mitigating dual-Doppler radar analysis errors (Davies-Jones 1979), extended out to about 75 km from the baseline. The dual-Doppler

radar analysis domain (shown in Fig. 1) was a 150 km \times 100 km area extending 15 km in the vertical. Three-dimensional kinematic fields were obtained by synthesizing the radial velocity measurements from the two radars within the analysis domain using NCAR Custom Editing and Display of Reduced Information in Cartesian space program (CEDRIC; Mohr et al. 1986). The procedure for dual-Doppler radar analysis on SCSMEX data was discussed in more detail by Wang (2004). It should be emphasized that the poor sensitivity of TOGA radar in the upper levels with weak reflectivity made it difficult to define the upper boundary condition. Therefore, an upward integration method, instead of the better variational or downward integration methods, was used to calculate the vertical air motion. As found from error estimation (Wang 2004), the derived vertical velocities are not reliable in the upper regions. To have a better picture of the case study, the derived vertical velocities will be shown in the whole vertical cross section. However, no conclusion will be made from the derived vertical velocities at high levels. Moreover, to filter noise in the vertical velocities, the horizontal wind fields derived from the dual-Doppler solution are lightly smoothed with a two-pass Leise filter (Leise 1981) prior to divergence calculation and vertical integration.

In addition to the radial velocity (V_R) measured by both radars for the dual-Doppler radar analysis, a set of polarimetric variables were also available from C-POL including differential reflectivity (Z_{DR}); total differential phase (Ψ_{DP}); and zero lag correlation coefficient between copolar horizontal and vertical polarized electromagnetic waves (ρ_{HV}). These polarimetric variables and specific differential phase (K_{DP}) calculated from Ψ_{DP} (Carey and Rutledge 2000) can be used to provide information on the size, shape, orientation, and thermodynamic phase of the hydrometers. Readers interested in a systematic discussion of these measurements and their applications may refer to Doviak and Zrnic (1993) and Bringi and Chandrasekar (2001).

An analysis of polarimetric radar-derived precipitation characteristics, including precipitation ice and liquid water content, was conducted using procedures similar to those outlined in Carey and Rutledge (2000) and Cifelli et al. (2002). As described in these earlier studies, a difference reflectivity (Z_{DP}) method (Golstani et al. 1989) was used to estimate the horizontally polarized reflectivity (Z_H) for both rain and ice separately. Rain Z_H^{rain} was estimated directly from observations of Z_{DP} , and ice Z_H^{ice} was then estimated as a residual (i.e., $Z_H^{\text{ice}} = Z_H^{\text{observed}} - Z_H^{\text{rain}}$). If the Z_{DP} -based method indicates the presence of mixed phase precipitation, then estimates of rainwater content (g m^{-3}) and

ice water content (g m^{-3}) are calculated using the following equations:

$$M_w = 3.44 \times 10^{-3} [Z_H^{\text{rain}}]^{4/7} (\text{g m}^{-3}), \quad (1)$$

$$M_{\text{ICE}} = 1000 \pi \rho_i N_0^{3/7} \left(\frac{5.28 \times 10^{-18} Z_H^{\text{ice}}}{720} \right)^{4/7} (\text{g m}^{-3}), \quad (2)$$

where Z_H^{rain} and Z_H^{ice} are in $\text{mm}^6 \text{m}^{-3}$, ρ_i is the ice density (917 kg m^{-3}), and N_0 ($4 \times 10^6 \text{ m}^{-4}$) is the intercept parameter of an assumed inverse exponential distribution for ice (Carey and Rutledge 2000). Note that Rayleigh scattering conditions are assumed. If the Z_{DP} -based method indicates the presence of pure rain (i.e., if the difference between observed Z_H and the estimated reflectivity associated with pure rain is less than the standard error, 0.9 dB), then it is assumed that the observed Z_H is dominated by water and the following equation from Bringi and Chandrasekar (2001) is utilized for estimating rainwater (M_w , g m^{-3}):

$$M_w = 0.60 \times 10^{-3} (Z_H^{0.85} \zeta^{-2.36}), \quad (3)$$

where $\zeta = 10^{(Z_{DR}/10)}$. When required in pure rain, rain-drop size (i.e., mass weighted mean diameter, D_m) was estimated using Z_{DR} according to $D_m = 1.619 * (Z_{DR})^{0.485}$ (mm) (Bringi and Chandrasekar 2001). If the Z_{DP} -based method indicates the presence of pure ice, then Eq. (2) is utilized, assuming $Z_H^{\text{ice}} = Z_H$. The rain rates for each radar volume were also calculated using an optimization technique with the parameters Z_H , Z_{DR} , and K_{DP} (Carey and Rutledge 2000). With this method, the measurement capability of each polarimetric variable is maximized. Combinations of those variables in rain-rate equations (Bringi and Chandrasekar 2001; Keenan et al. 2001) are described in Table 1. As discussed in Cifelli et al. (2002) and Carey and Rutledge (2000), the liquid and especially ice water contents reported herein are only approximate, since a number of assumptions were required. Given typical measurement error in the C-POL radar (i.e., Z_H : $\pm 1 \text{ dB}$; Z_{DR} : $\pm 0.2 \text{ dB}$; K_{DP} : $\pm 0.3 \text{ km}^{-1}$). The expected normalized standard errors for the various estimated microphysical parameters are given in Table 2 (Bringi and Chandrasekar 2001; Carey and Rutledge 2000).

3. Synoptic situation and environmental features

The satellite infrared image for 0600 UTC (UTC = LST - 0800) 24 May (Fig. 2) revealed a mesoscale convective system (MCS) over the southern coast of China and the sea to the south. This cloud cluster originated over the southwestern China and northern Indochina peninsula around 1200 UTC 22 May. In the next 36 h, the MCS drifted slowly to the east following the prevailing westerly winds associated with a trough

TABLE 1. C-POL rain-rate estimation.

Conditions:	
(a)	$Z_{DR} \geq 0.5$ dB
(b)	$Z_H \geq 35$ dB and $K_{DP} \geq 0.5^\circ \text{ km}^{-1}$
Equations:	
1. Both conditions (a) and (b) are satisfied:	$R(K_{DP}, Z_{DR}) = 37.9 \times 10^{-0.072 Z_{DR}} (K_{DP})^{0.89}$
2. Only condition (a) is satisfied:	$R(Z_H, Z_{DR}) = 0.0058 \times 10^{-0.209 Z_{DR}} (Z_H)^{0.91}$
3. Only condition (b) is satisfied:	$R(K_{DP}) = 32.4 \times (K_{DP})^{0.85}$
4. None of condition (a) or (b) is satisfied:	$R(Z_H) = 0.015 \times (Z_H)^{0.734}$

to the south of the Tibetan Plateau. On 24 May, the MCS started to propagate southeastward and offshore with a major portion over the SCS region. Ahead of the MCS, there was a broad clear area extending northeast all the way to Japan. The synoptic situation for 1200 UTC 24 May 1998 is summarized in Fig. 3. After the completion of the SCS summer monsoon onset at low levels by 20 May (Wang 2004), the low-level airflow in the northern South China Sea was dominated by southwesterly monsoon flow (Fig. 3a). Except for the eastern end of the SCS controlled by the retreating subtropical high, most of the northern SCS region exhibited a relative humidity over 70%, another indicator of the summer monsoon onset. At 850 hPa, a mesovortex centered at 21°N, 115°E was evident near the southern coast of China. The disturbance strengthened the southwesterly winds in the northern SCS to bring in more warm air. Moreover, the mesoscale vortex helped the development of low-level moisture convergence that is a key element for the genesis of mesoscale convection (e.g., Cotton and Anthes 1989). At 500 hPa, the SCS observation domain was ahead of a moderate trough controlled by southwesterly winds (Fig. 3b). At the upper level (200 hPa), there was a large anticyclone centered near 18°N, 108°E. An area of diffluence occurred over the northern SCS to the northeast of the anticyclone. Overall, the synoptic-scale low- and upper-level disposition provided a favorable environment for the development of convection.

On 24 May, there were three squall lines (Fig. 4) observed by the SCSMEX radar network (more details in section 4). Wind and thermodynamic soundings, rep-

TABLE 2. Estimated normalized standard error of microphysical quantities.

Microphysical quantities	Normalized standard error
D_m	10%–20%
$R, M_w [Z_H, Z_{DR}, K_{DP}]$	10%–35%
$R, M_w [Z_H]$	30%–70%
$M_{ICE} [Z_H]$	50%–100%

resentative of the prestorm environment at 1200 UTC, 3–4 h prior to the passage of the first squall line, and at 1800 UTC, 2–3 h ahead of the arrival of the second squall line, are summarized in Fig. 5. At 1200 UTC, moisture was available at low levels. A dry layer was found at the mid- to upper levels over 500 hPa, with a maximum dewpoint depression over 25°C around 400 hPa. This type of dry midlayer air was often observed during the SCS monsoon onset (15–25 May; Johnson and Ciesielski 2002; Wang 2004). The sounding exhibited conditional instability. Average virtual potential temperature and water vapor mixing ratio values in the near-surface layers were used to calculate the convective available potential energy (CAPE). The CAPE was low at about 750 J kg⁻¹ showing weak instability. The lifting condensation level (LCL) was at 941 hPa, while the level of free convection (LFC) was at 646 hPa. From the low to midlevels, the favorable wind speed shear was apparent and can be categorized as a quasi-straight or unidirectional hodograph (not shown). The moderate low-level wind shear (800–1000 hPa) was southeastward at 8.7 m s⁻¹ or about 4.4 m s⁻¹ km⁻¹.

At 1800 UTC, the most pronounced change occurred at the midlevel with the moistening of the dry layer. A relative dry layer was located above 420 hPa, but with reduced magnitude. At the low to midlevels, the temperatures were generally lower than those 6 h earlier. This could be related to the ice melting and evaporative cooling associated with the passage of the first squall line. The CAPE increased significantly to over 1500 J kg⁻¹, comparable to those for the GATE (Zipser and LeMone 1980) and TAMEX (Jorgensen et al. 1991). The increased CAPE seems to be the result of either destabilization of the sounding by convergence accompanying the first squall line or less stable air coming with the mesovortex. Compared to the sounding taken 6 h earlier, the direction and magnitude of the low-level wind shear remained the same, while the LCL and LFC lowered to 954 and 826 hPa, respectively. Obviously, after the passage of the first squall line, the environmental conditions were more favorable for the development of organized deep convection.

4. The evolution and propagation of the squall-line system

The squall-line system including several lines persisted from 1200 UTC 24 May to 0500 UTC 25 May. The early convective echoes appeared at about 1200 UTC as several individual newly formed convective cells. These small cells lined up in a discontinuous arc-shaped convective line about 50 km west of the C-POL radar (Fig. 4a). The north–south orientation of the convective line is perpendicular to the low-level wind shear

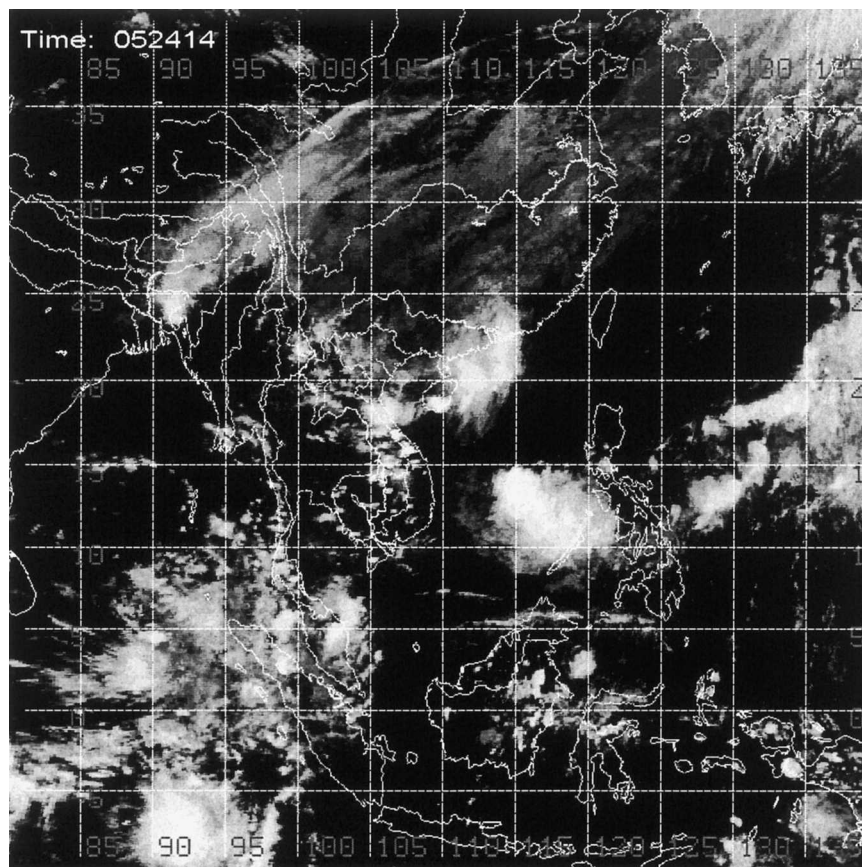


FIG. 2. Infrared imagery from *Geosynchronous Meteorological Satellite-5* (GMS-5) at 0600 UTC 24 May.

(1000–800 hPa). This was consistent with the studies on western Pacific convection by LeMone et al. (1998) who found the orientation of the convection tends to be perpendicular to the low-level (surface to 800 hPa) wind shear if its magnitude is over 4 m s^{-1} . While moving eastward, this convective line gradually intensified into a broader, stronger, and more organized squall line. This squall line reached its climax both in size and intensity near 1600 UTC. The peak reflectivity of 50 dBZ was recorded with the echo top at 12 km MSL.

Along with the decay of the first squall line, a new and intense convective line started to develop about 40 km behind the original squall line (Fig. 4b). Compared to the echoes in the first squall line, the main echo of the second squall line at its early stage was more intense with larger area coverage. At 2200 UTC, the second squall line was at its mature stage showing a continuous convective band with the east–west extension up to 50 km. The peak radar reflectivity of about 55 dBZ was recorded at 1.5–3.0 km MSL. Overall, the second squall line was larger and more intense than the first squall line. With the echo top reaching 15 km MSL, the second squall line was also the tallest convection observed

on 24 May. There are two factors that may explain why the second squall line was a much more intense line than the first one. First, from the soundings taken at Dongsha Island before and after the passage of the first squall line (Fig. 5), the postline environmental conditions had a much higher value of CAPE. Second, after the initiation near midnight, the second line developed throughout the early morning hours, when the diurnal cycle of the convection over the open ocean reached its most active period (Gray and Jacobson 1977). The mature phase of the second squall line lasted for several more hours until 0400 UTC 25 May and started to dissipate afterward (not shown).

About an hour later, after the formation of the second squall line to the northwest, several new cells developed and lined up in a northeast–southwest direction about 80 km behind the second squall line at 1800 UTC. These cells formed a more continuous convective line later and became the third squall line observed on 24 May. However, after 2200 UTC when the second squall line was at its mature phase, the third squall line to the west weakened to a short line and dissipated in the next hour or so. In contrast to the second squall

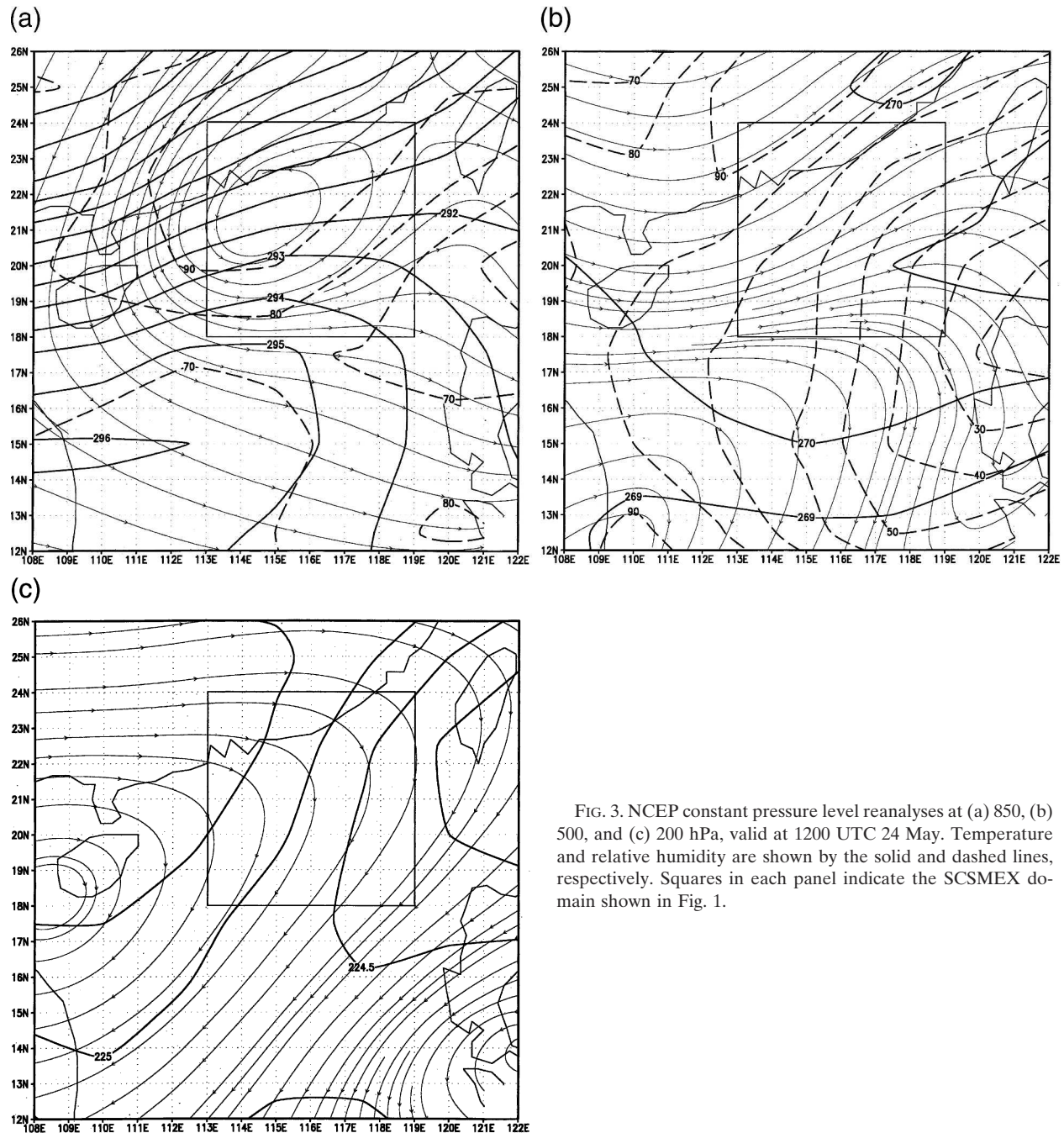


FIG. 3. NCEP constant pressure level reanalyses at (a) 850, (b) 500, and (c) 200 hPa, valid at 1200 UTC 24 May. Temperature and relative humidity are shown by the solid and dashed lines, respectively. Squares in each panel indicate the SCSMEX domain shown in Fig. 1.

line, the third squall line did not become a well-organized line with significant intensity before its dissipation. Without enough data around the third line or between the second and third line, we are not sure about the cause for the dissipation of the third line. However, considering that the third line was just a few tens of kilometers behind the mature and intense second line, we believe that the effects of the second line may have played a role in this process. For instance, the mesoscale descending motion often detected after the passage of

strong convection may suppress the maintenance of updrafts and result in the weakening of the third line.

5. Precipitation and kinematic structure

In this section, the precipitation and kinematic structure of the second squall line, the most intense and well-organized one, will be discussed. During its mature phase, the second squall line was located in the dual-Doppler radar analysis lobes, which is ideal for a detailed study of its kinematic structure. The first squall line was

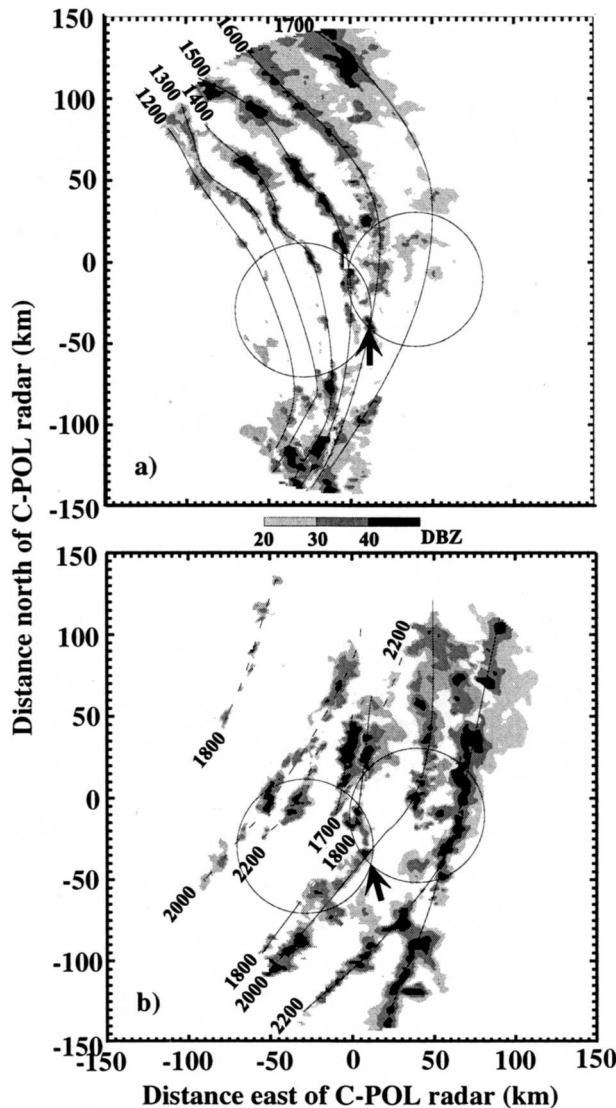


FIG. 4. Time series of the C-POL radar reflectivity (dBZ) at 2.5 km MSL for the evolution of the main echoes of (a) the first squall line, and (b) the second (solid line) and third (dashed line) squall lines on 24 May. Arrows indicate the position of soundings shown in Fig. 5.

only in the western dual-Doppler lobe during its developing phase. When it reached its climax near 1600 UTC, the first squall line was too close to the radar baseline to conduct dual-Doppler synthesis. The third squall line did not enter the dual-Doppler lobe until it started to weaken.

We have performed 5-h of dual-Doppler radar analysis from 1900 to 2350 UTC when the main part of the second squall line was in the dual-Doppler analysis lobes. After carefully examining the 30 volumes from both the C-POL and TOGA radars, we present the results from 2040 UTC as a typical example to illustrate the horizontal and vertical structure of the second squall line at its mature phase, while the central part of

the squall line was ideally located at the center of the dual-Doppler lobe.

At 2040 UTC, as shown in Fig. 6a, the mature squall line showed a continuous convective line in the eastern dual-Doppler lobe. It included several convective cores lining up on the north–south direction with radar reflectivity over 40 dBZ. The principal cells had an east–west extension of 20–30 km. At 1.5 km, during the highly linear phase of the squall line the horizontal circulation was predominantly two dimensional. The system-relative flow in the line was uniformly from the front to the rear of the system. The inflow was stronger in the principal cells at a speed of $5\text{--}6\text{ m s}^{-1}$. Considering the speed of the squall line at 5 m s^{-1} to the east, this front-to-rear flow matched the weak westerly flow shown at 850 hPa in the environmental sounding (Fig. 5). In other words, the system-generated flows at the low levels were mainly in the rear part of the system. The low-level inflow exhibited a remarkable deceleration at the rear edge of the squall line. This also formed a fairly uniform and strong region of low-level convergence there (not shown).

Updrafts at 1.5 km MSL were mostly oriented in a band just behind the reflectivity maxima associated with those convective cells (Fig. 6b). The squall lines had the maximum radar reflectivity, low-level convergence, and updrafts at the rear part of system. Downward motion was generally ahead of the updrafts in the front portion of the system between the principal convective cells. This was an indication of a descending rear-to-front outflow. Similar kinematic structure was also observed in the developing stage of the first squall line (not shown). The kinematic structure retrieved here was atypical compared to most studies on tropical and subtropical squall lines in the Pacific prior to SCSMEX [e.g., Wang et al. 1990 (TAMEX); Keenan and Rutledge 1993 (Australia); Jorgensen et al. 1997 (western Pacific)]. In those previous studies, the tropical and subtropical squall lines were found to have a narrow leading edge in the front of the system with the maximum radar reflectivity. The maximum low-level convergence and updrafts were in the form of narrow ribbons and usually located just ahead of the reflectivity maximum. Behind the strong updrafts, there was larger area with downward motion as a result of descending rear to front outflow. On the other hand, in a case study of an MCS occurring at the beginning of the SCS summer monsoon onset, Wang (2004) found maxima in reflectivity and updraft in the rear of the system with downdrafts ahead of them similar to the structure found on 24 May. We believe that this type of atypical structure of monsoonal convection is actually quite normal during the onset stage of the SCS summer monsoon.

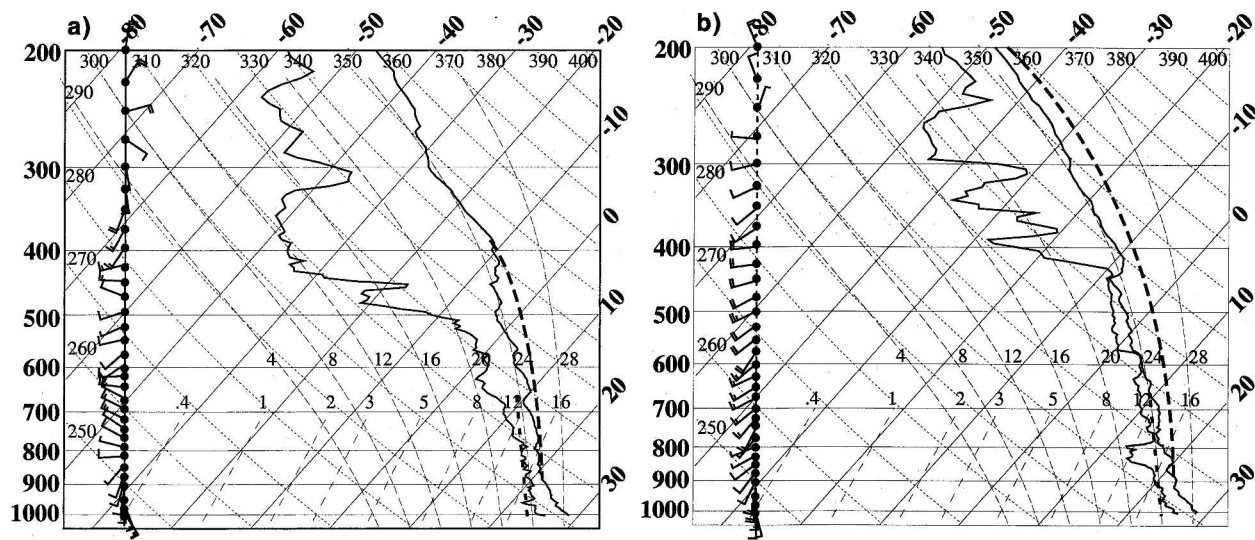


FIG. 5. Sounding launched from *Shi Yan-3* at (a) 1200 and (b) 1800 UTC 24 May 1998. Hypothetical parcel ascent trajectories (dashed lines) and downdraft path (dotted lines) are also plotted.

Moreover, the size and shape of the low-level updraft zone for the squall lines observed herein were different from those observed in previous studies. Instead of being limited to a narrow ribbon-shaped area, this system had an updraft in a wider rear region with relatively irregular shape. In addition to the cellular-shaped updraft zone mostly at the rear, there was an elongated updraft band partially crossing the line. The magnitude of the updraft at 1.5 km was about 2 m s^{-1} with the downdraft at around 1 m s^{-1} to the east. The analysis of Z_{DR} at 1.5 km also exhibited a reversed structure to most typical tropical squall lines. In typical tropical oceanic (Atlas and Ulbrich 2000) and tropical continental (Cifelli et al. 2000) squall lines, a narrow (2–5 km) zone of mid to large (1.5–3 mm) raindrops is usually found within warm ($T > 0^\circ\text{C}$) updrafts at 1–3 km MSL in developing convective cores at the leading edge. However, in the present case, several Z_{DR} maxima over 1.5 dB were located along the trailing edge of the squall line (Fig. 6b). More discussion on this atypical structure of the squall line will be given below along with the results from the vertical cross sections. At upper levels, only the two principal cells of the squall line reached the 9 km MSL with radar reflectivity up to 30 dBZ (Fig. 6c). The eastward shift of the cells from the low level indicated an eastward-sloping updraft. The airflow was from rear to front, in the opposite direction of low-level inflows. The shape of the updraft was more cellular with maximum vertical velocities of 7 m s^{-1} . The convective downdraft was also evident ahead of the updrafts.

The vertical cross sections of radar reflectivity, differential reflectivity, system-relative wind, and vertical velocity across the two principal cells are shown in Fig.

7. The echo top reached 14–16 km MSL. Although not shown in our interpolation, the actual maximum radar reflectivity recorded was about 55 dBZ. An important characteristic of this squall line, also discussed earlier with horizontal cross sections, was that the front-to-rear low-level inflow extended all the way to the very rear part of the cell. The deceleration of the low-level inflow from the front portion was also evident. In the southern cell (Fig. 7c), the formation of a new cell behind the old cell was apparent. The low-level maximum updraft was also located in the convection zone at the rear of the system (Figs. 7b,d). This type of strong updraft at the rear also implied that the inflow must pass a region ahead of the convective line before entering the convective tower. Theoretically, this type of structure may have some negative effects on the development and maintenance of the deep convection. When the inflow passes through the convective precipitating area, it could be chilled by the cool air created by evaporative cooling. As a result, the buoyancy of the air in the updraft might be reduced. Consequently, the intensity of the updraft and the convection might weaken as well. Nevertheless, from a simple 2D numerical simulation, Parker (2002) argued that evaporative cooling actually occurs over a relatively deep layer with cooling increasing with height over the lowest 2–2.5 km. Therefore, the net effects of this process are to further destabilize the low levels and result in an increased CAPE. The maximum updraft was about $5\text{--}7 \text{ m s}^{-1}$ at an elevated height of 9–10 km MSL (Figs. 7b,d). Downdrafts were located just ahead of the updrafts. Consistent with the weaker updrafts in a tropical oceanic environment, there was a sharp reflectivity gradient above the 0°C level.

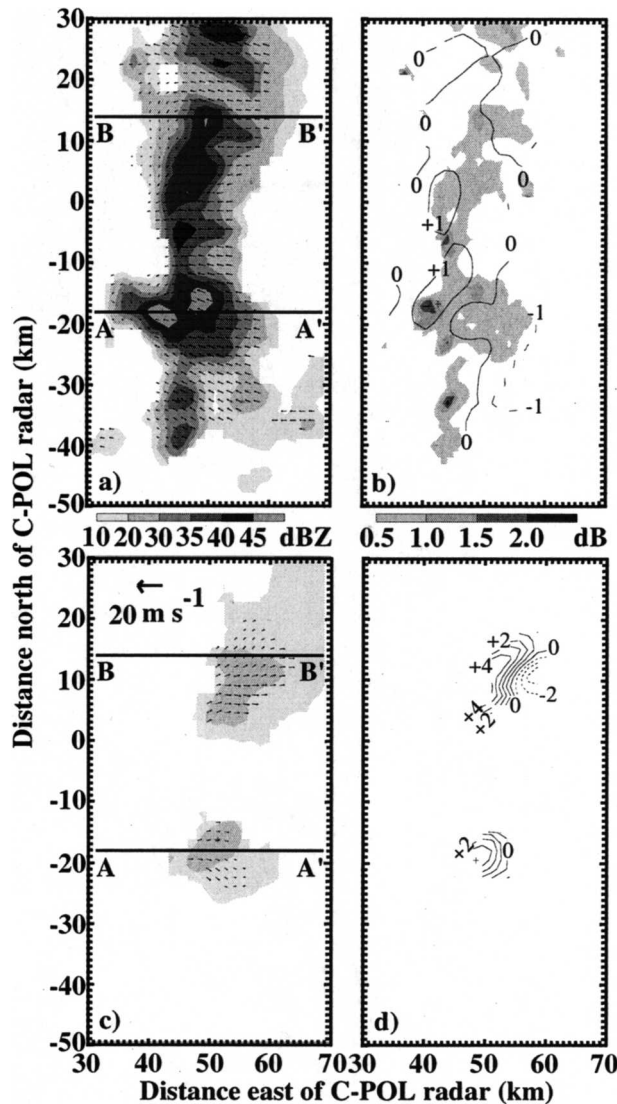


FIG. 6. (a) Radar reflectivity (dBZ) and system-relative wind flow, and (b) differential reflectivity (dB, shaded) and vertical air motion (m s^{-1} , contoured) at 1.5 km MSL valid at 2040 UTC. (c), (d) Same as (a), (b), respectively, except at 9.0 MSL with no differential reflectivity displayed. The 20 m s^{-1} scaling vector for winds is shown in the upper-left corner in (c).

Despite radar reflectivity over 50 dBZ, both the first and second squall line had little stratiform precipitation accompanying the convective portion. Using a partitioning algorithm based on Steiner et al. (1995), we found that the stratiform area on 24 May accounted for only 10%–15% of the total rain area. This was far less than the overall 63%–70% stratiform occurrence during four TRMM field experiments in the Tropics (Tokay et al. 2001). The environmental soundings (Fig. 5) clearly showed that the mid- to upper-level air was quite dry. As determined from modeling studies by W.-K. Tao (NASA GSFC, 2002, personal communica-

tion), the dry air in the mid- to upper levels generally results in a rapid evaporation of the stratiform cloud after the passage of its convective counterpart. The effects of dry air aloft on the stratiform rain development are more significant in the tropical oceanic region than in a midlatitude continental environment. In a midlatitude continental circumstance, the convective induced updrafts could be much stronger than that in a tropical oceanic area. Therefore, the deleterious microphysical effects of evaporation in a dry environment may be overcome by the convectively driven mesoscale circulation. With enough low-level moisture and buoyancy, the pronounced updrafts may advect hydrometeors to moisten the dry environment and result in the formation of stratiform rain. As a result, extensive stratiform regions may be observed in an environment with dry mid to upper layers (e.g., Houze 1993). However, for the tropical squall-line case studied here, the vertical velocities at the cloud base ($1\text{--}2 \text{ m s}^{-1}$, Fig. 7) were weak and the buoyancy was limited (Fig. 5). Both of these factors prevented the system from generating stratiform regions. In addition, the weak system-relative upper-level winds may also play a role in minimizing the scale of stratiform rain by failing to advect hydrometeors away from the convective cores. In fact, there was no long-lasting stratiform rain with considerable area coverage on 24 May.

The only signs of stratiform rain formation could be found in the vertical cross section across the intense northern cell (Fig. 7a). There was a nose of weak reflectivity area at around 8 km MSL ahead of the leading edge of the squall line. A forward tilt of roughly 40° from the horizontal was seen in both the vertical airflow and reflectivity contours in the cross section. The forward tilt of radar reflectivity indicated the tendency of stratiform rain ahead of the system. There was also a small local reflectivity maxima at about 4.5 km just below the eastward-leaning reflectivity contour. This midlevel reflectivity maximum, or radar bright band, was a clear sign of stratiform rain and marked the position of the melting layer. From most previous observational (LeMone et al. 1984; Jorgensen et al. 1997) and modeling (Trier et al. 1996, 1997) studies, it was found that a rearward tilting of the inflow was more common and usually resulted in a stratiform region trailing the convective part. Rotunno et al. (1988) illustrated the important role of the cold pool in shaping the structure of the squall line by balancing the horizontal vorticity of the low-level shear. When a cold pool dominates the circulation, the circulation progressively leans farther upshear, that is, forming a trailing stratiform region. On the other hand, in the presence of a weak cold pool, an updraft/thermal will tilt downshear, that is, forming a

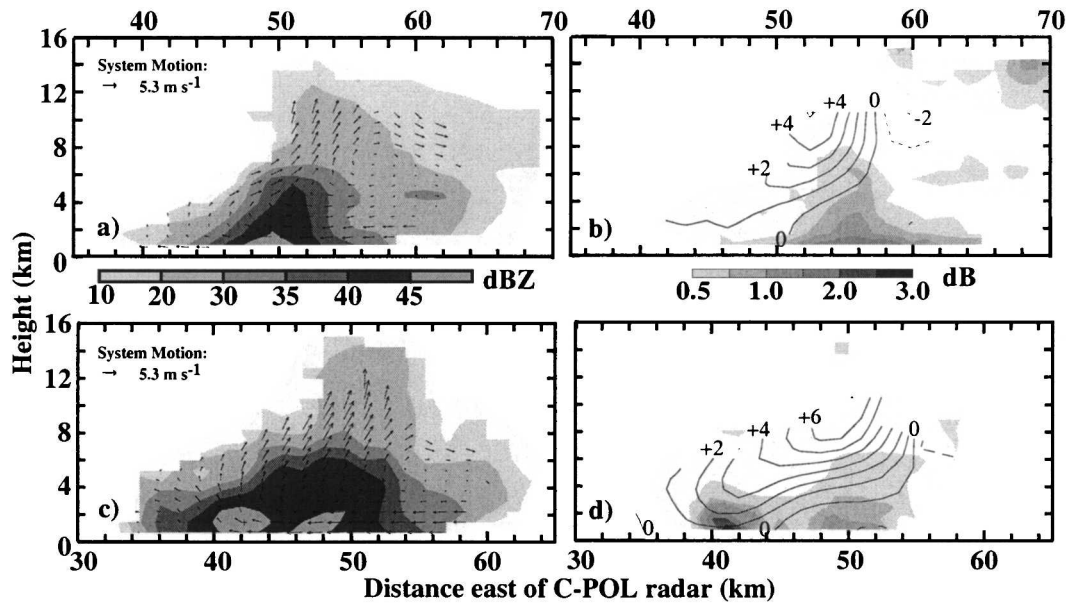


FIG. 7. Vertical cross section of (a) radar reflectivity (dBZ) and system-relative wind flow, and (b) vertical air motion (m s^{-1} , contoured) and differential reflectivity (dB, shaded) along BB' in Fig. 6 valid at 2040 UTC. (c), (d) Same as (a), (b), respectively, except along AA' in Fig. 6.

leading stratiform region. In other words, if the horizontal vorticity associated with the cold pool resulting from evaporation is insufficient to counteract the circulation driven by lower-tropospheric vertical shear, the downshear tilt of the convection and the leading stratiform region would form. Although the lack of the in situ thermodynamic measurements in this study makes it difficult to determine an accurate intensity of the cold pool, an analysis of the environmental soundings (Fig. 5) may provide a reasonable estimation of the contribution from evaporative cooling in downdrafts. Usually, the downdraft originates near the level of minimum wet-bulb potential temperature about 3–5 km above the ground. The downdraft path assuming sufficient rainwater to maintain saturation for the entire descent can be estimated by following the moist adiabatic processes, that is, the wet-bulb potential temperature curve on a thermodynamic diagram, to the surface. The maximum cooling is the temperature difference between the downdraft air and the environmental air at the surface. However, if the air descends subsaturated, the parcel temperature will be greater than its wet-bulb temperature and the cooling will be less. For the present case, the possible maximum cooling was only about 4°–5°C (Fig. 5). This suggested that a downdraft-produced cold pool with sufficient strength to produce an upshear-tilted convection was unlikely.

Another difference of the current case from the previous observations (Roux 1988; Jorgensen et al. 1997) and simulations (Trier et al. 1997; Robe and Emmanuel

2001) of tropical squall lines was the lack of a pronounced environmental low-level jet. The absence of the low-level jet removed the reverse shear above the jet that may support the rearward advection of warm and moist air above the cold pool. That rearward advection discussed in previous literature may further strengthen the vertical distribution of buoyancy associated with midlevel convergence and upper-tropospheric ascent, and therefore help the development of stratiform rain in the trailing regions (Houze 1993). In a climatological study, Parker and Johnson (2000) found that the trailing or paralleling stratiform rain occurs in over 80% of convective lines observed in the midlatitudes over the United States, while the leading stratiform cases only account for 19%. However, combining the analysis in this study and the previous SCSMEX study by Wang (2004), leading stratiform mode convection seems very common during the onset period of the SCS summer monsoon.

6. Rainfall and hydrometeor characteristics

Cross sections of Z_{DR} for the intense cells sampled at 2040 UTC are also shown in Figs. 7b,d. In general, Z_{DR} columns were constrained to relatively low levels. The contour of 1 dB was found in the lowest 3 km, well below the 0°C level. This indicated that oblate drops with diameter over 1.5 mm only existed in the lower levels and were not lofted into the mixed-phase region. Our results shown here had some similarity to the TRMM–LBA westerly case (Cifelli et al. 2002),

However, the raindrops were less oblate (and hence smaller) and limited to even lower levels. For the convective cells at their mature phase (the northern cell in Fig. 7b and east of the southern cell in Fig. 7d), the mid-sized raindrops indicated by Z_{DR} of 0.5–1.0 dB reached the level of 6 km. When the mid-sized drops were lofted to midlevels, they followed the updraft track toward the leading edge and then were slowly sorted out by size toward the front of the convection. Elevated Z_{DR} (>0.5 dB) collocated with low Z_H (<30 dBZ) at heights of 6 km and higher in the forward anvil region of both Figs. 7b,d were likely associated with horizontally oriented ice crystals or aggregates of ice crystals.

For the new developing cell in the west of the southern cell, the maximum Z_{DR} reached about 3 dB at the lowest levels corresponding to drops of about 2.8 mm in diameter (Fig. 7d). The location of the maximum Z_{DR} matched the position of maximum low-level updrafts derived from dual-Doppler analysis (Fig. 7c). At the lowest levels, the contours over 1.5 dB had a front-to-rear slope with height corresponding to the backward updraft. However, even with a maximum Z_{DR} of 3 dB, the 1-dB contour only reached up to 3 km. This suggests that the large, oblate raindrops immediately fell out because of relatively weak updrafts at low levels. The mid-sized raindrops with Z_{DR} of 0.5–1.0 dB followed a trajectory straight upward between the levels of 3–4.5 km. At this developing stage, the mid-sized particles were concentrated only at low levels. Compared to other analysis of tropical MCS [e.g., in the Maritime Continent by Carey and Rutledge (2000) and the Amazon by Cifelli et al. (2002)], the height and magnitude of the Z_{DR} column shown here were quite low. At the onset stage of the SCS summer monsoon, the low-level convergence and updrafts associated with the convection were relatively weak and not sufficient to lift hydrometers aloft to subfreezing temperatures, for example, to the level of the mixed phase. For the case studied here, the low-level inflow had to pass a downdraft and cooled region before entering the updraft. Modified air in the low-level updraft may have reduced the buoyancy and hence updraft speed, contributing further to a low height and magnitude of the Z_{DR} column.

Representative cross sections of rainwater content for the intense southern cell (Fig. 8) exhibited comparable maxima in the developing (e.g., 4 g m^{-3} at 41 km east of C-POL) and mature (e.g., 3.5 g m^{-3} at 49 km east of C-POL) cells at low-levels (2 km MSL). However, analysis of Figs. 7 and 8 reveals that the kinematic and microphysical processes leading to these maxima at different stages of the convective life cycle were somewhat distinct.

In the developing cell, the maximum water content of

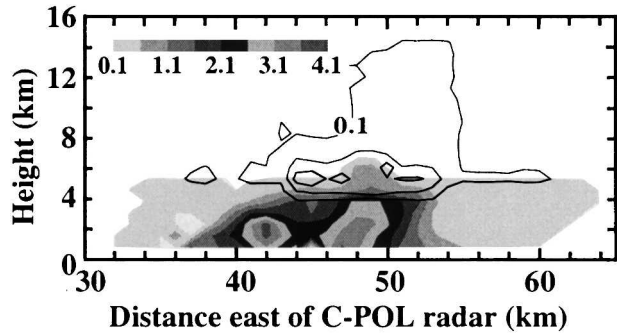


FIG. 8. Vertical cross section of rainwater content (g m^{-3}) (shaded) and precipitation ice water content (g m^{-3}) (contoured at 0.1, 0.6, and 1.1) along AA' in Fig. 6.

over 4 g m^{-3} was located at 1.5–2.5 km MSL above the maximum Z_{DR} at the lowest level. The gentle low-level updrafts allowed sufficient time for the collision-coalescence process to develop both large raindrops and high rainwater contents. However the weak low-level updrafts were unable to lift the largest raindrops found at the lowest level farther upward. Those large drops with mean mass-weighted diameter (D_m) of 2.0–3.0 mm were offset below the maximum water content due to size sorting by the updraft. It was the drops with D_m of 1.5–2.0 mm at around 2 km MSL that contributed to the maximum rainwater content in the developing convective core. Given the very weak updrafts at 3–5 km MSL, there was no indication of the lofting of raindrops above the freezing level in the developing convection. As a result, there is very little precipitation ice mass in the developing cell. The lack of significant raindrop freezing also denied the extra buoyancy that is contributed by the latent heat release of freezing to the growing cells. This behavior is in stark contrast to tropical continental convection, which typically exhibits vigorous lofting of supercooled raindrops in the strong low-level updrafts, and the initial production of large quantities of precipitation ice mass (i.e., frozen drops) during the developing stage (Carey and Rutledge 2000; Cifelli et al. 2002). On the other hand, the precipitation structure of the developing cell over the SCS was similar to the maritime-like convection over the “green ocean” of the Amazon during the low-level westerly wind regime (Cifelli et al. 2002).

In the mature cell, the low-level updrafts were still weak, promoting continued warm rain processes, but large raindrops ($D_m > 2 \text{ mm}$) had already precipitated out since the updrafts were unable to keep them aloft. As a result, the maximum rainwater content up to 3.5 g m^{-3} was collocated with the maximum Z_{DR} (1.0–1.2 dB or $D_m = 1.6$ –1.8 mm) at the lowest level. Midlevel updrafts were larger in the mature as compared to the developing convection and were capable of lofting a

small zone of supercooled raindrops about 1 km above the freezing level (e.g., Fig. 8 at 49 km east of CPOL). Freezing of the supercooled drops caused a slight enhancement in the precipitation ice mass (0.6 to 1.2 g m^{-3}) at midlevels (5–6.5 km MSL) in the mature cell. However, the vertical extent of the Z_{DR} column (Figs. 7d, 10) was modest and hence supercooled drops and enhanced precipitation ice mass associated with frozen drops were present only in the lowest (or warmest) portions of the mixed-phase zone. As noted before, the mature convection is similar in this regard to the maritime-like convection over the Amazon during the westerly wind regime and very unlike the vigorous tropical continental convection during the easterly regime of the Amazon (Cifelli et al. 2002) and the tropical island convection studied by Carey and Rutledge (2000), which were both characterized by strong and vertically extensive Z_{DR} columns and hail/frozen drop zones. The frozen drops likely fell through the updraft in the mature cell, melted, and hence contributed to the rainwater maximum at lower levels. As a result, rain at later stages of convection on 24 May was likely the combination of both warm and modest mixed-phase precipitation processes.

In general, very few raindrops were lofted above the freezing level and precipitation-sized ice was scarce on 24 May. Therefore, only those smallest particles were observed at high levels (echo top up to 15 km in Fig. 7c). Due to the dry air at the upper levels, those ice particles might actually evaporate or sublimate and never hit the ground. This also likely explained the lack of stratiform rain on 24 May. By comparison, stratiform rainfall was widespread in the green ocean convection over the Amazon during the westerly regime (Cifelli et al. 2002). The key difference appears to be the relative lack of dry air in the 500–200-hPa layer and hence evaporation/sublimation during the westerly regime of Amazonian convection (Halverson et al. 2002).

7. Composite vertical structure

In this section, mean profiles and contoured frequency by altitude diagrams (CFADs; Yuter and Houze 1995) are used to present statistically the characteristics of the squall lines observed on 24 May. The CFAD summarizes frequency distribution information about a variable in a given radar echo volume. It is a convenient tool to display multiple histograms in a two-dimensional format. The relative frequency of occurrence of a given parameter in the area of detectable echo can be shown at each height. Comparison of the reflectivity distribution, system-relative winds, and polarimetric measurements with the other subtropical and tropical convection documented in the literature are made to describe the characteristics of the squall line

occurring during the late stage of the SCS summer monsoon onset.

The CFADs and mean profiles of reflectivity at 1550 and 2140 UTC, when the first and second squall line reached their peak stage, respectively, are shown in Fig. 9. The second squall line was apparently taller and more intense than the first one. The echo top of the second squall line reached 16 km MSL, comparing to 14 km MSL for the first squall line. The mean reflectivity profile at the lowest level was just over 30 dBZ for the first squall line, and near 40 dBZ for the second squall line. Both squall lines had a slowly decreasing mean reflectivity with increasing height near the melting layer. A sharp decrease of mean reflectivity was evident from 5 to 8 km MSL above the melting layer, consistent with the weak updrafts in the Tropics (Zipser 1977). This decrease was more pronounced at 1550 UTC indicating even weaker updrafts for the first squall line. The decrease of mean reflectivity slowed again in the layers above 8 km MSL. In general, the overall mode of the mean reflectivity profile for both squall lines on 24 May was very similar to the tropical oceanic MCS events summarized by Jorgensen and LeMone (1989) and Zipser and Lutz (1994). At 2–4 km MSL, the occurrence of reflectivity over 40 dBZ, an indicator of intense convection, was over 10% at 2140 UTC, but far less than that frequency at 1550 UTC. At upper levels, the convection at 2140 UTC also had a significantly higher frequency of occurrence of intense echo features. The probability of occurrence of 30-dBZ echo fell below 1% at about 9 km MSL at 2140 UTC compared to 6 km MSL at 1550 UTC. DeMott and Rutledge (1998) suggested that the rainfall production is larger for radar echoes with higher maximum 30-dBZ echo heights. Supporting their argument, our calculation showed that convective rain rates in the first squall line at 1550 UTC were about $55\text{--}65 \text{ mm h}^{-1}$, while rain rates of the convective cores in the second squall line at 2140 UTC reached up to $80\text{--}90 \text{ mm h}^{-1}$.

To examine the statistical kinematic structure of the squall line, we also present, in Fig. 10, the mean profiles and CFAD diagrams of system-relative u component, v component, and divergence at 2040 UTC, when a detailed dual-Doppler analysis was performed for the mature stage of the second squall line. The negative u -component dominated at low levels. Since the system moved eastward, this indicated a front-to-rear low-level inflow. The mean inflow speed was at 5 m s^{-1} at the lowest level and decreased with increasing height. The mean profile of the u component turned to be positive at levels above 4 km MSL. The upper-level outflow reached a maximum at about 9 km MSL. The CFAD diagram further supported the observation from the

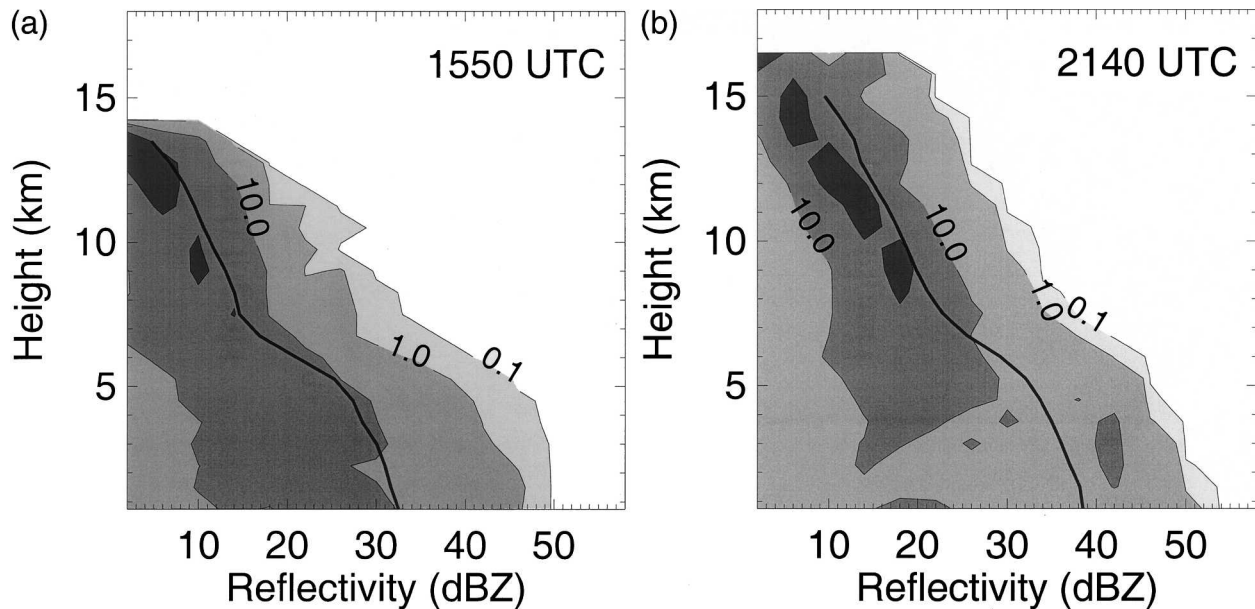


FIG. 9. CFADs and mean profiles of radar reflectivity at (a) 1550 and (b) 2140 UTC 24 May. Bin size is 4 dBZ.

vertical cross section (Fig. 7), that is, the squall line had an uncommonly strong rear-to-front outflow. The mean profile of the v component shows a weak system-relative flow along the squall line. The most frequent occurrence ($>30\%$) of the v component was near zero

or slightly positive. The magnitude of the mean v component was less than 1.5 m s^{-1} throughout the system. As discussed before, the vertical velocity at higher elevations contained uncertainties when using upward integration as a result of the hard to define upper bound-

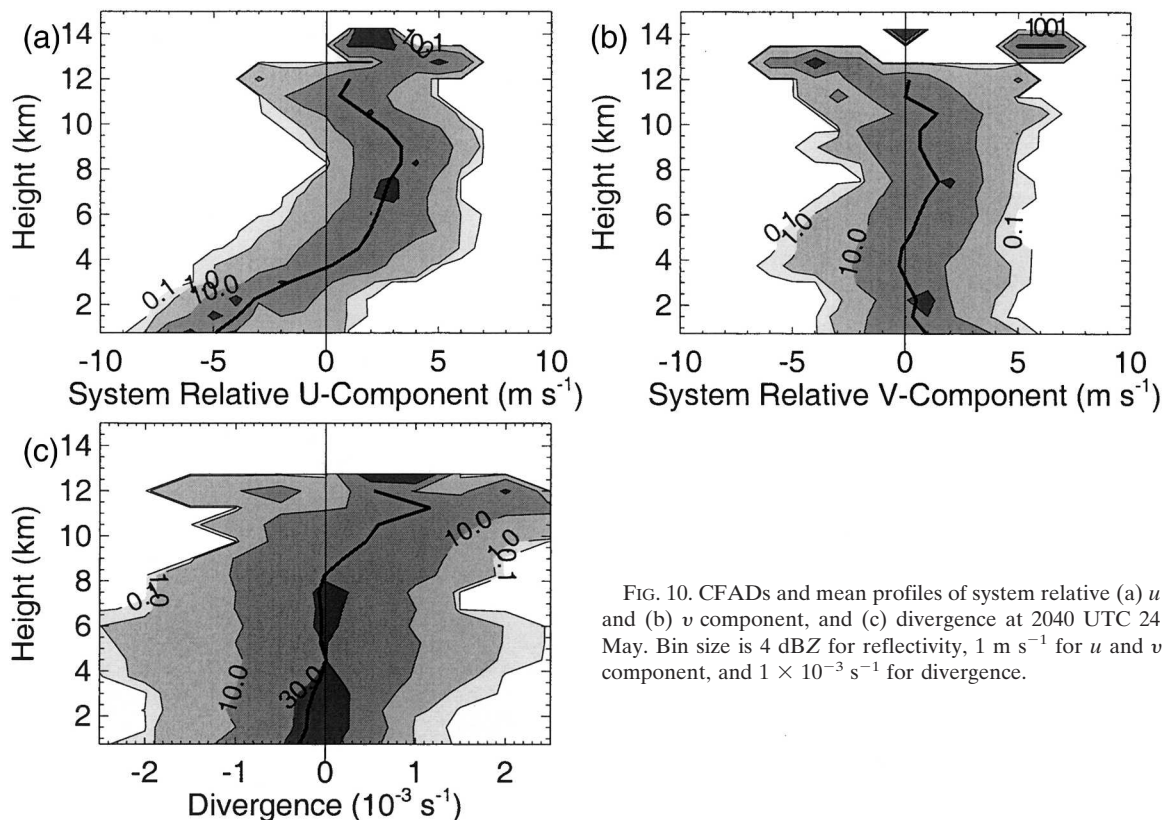


FIG. 10. CFADs and mean profiles of system relative (a) u and (b) v component, and (c) divergence at 2040 UTC 24 May. Bin size is 4 dBZ for reflectivity, 1 m s^{-1} for u and v component, and $1 \times 10^{-3} \text{ s}^{-1}$ for divergence.

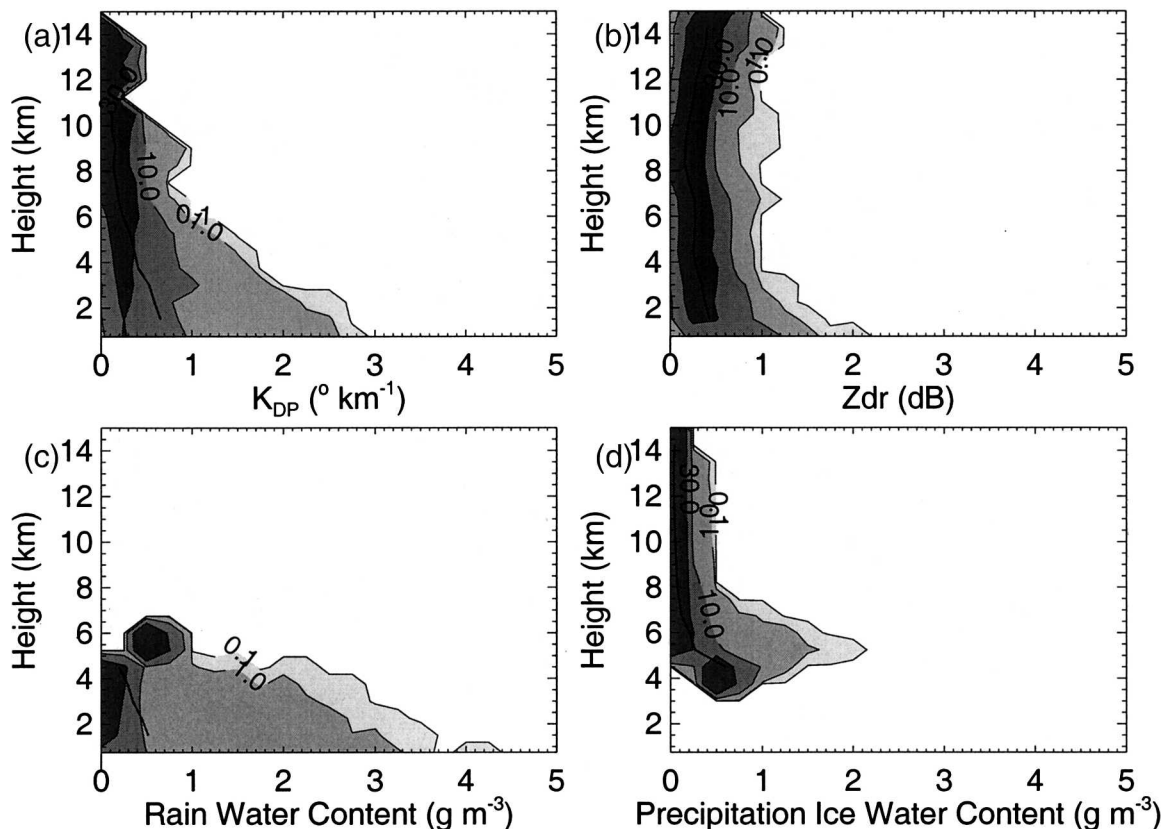


FIG. 11. CFADs and mean profiles of (a) specific differential phase ($^{\circ} \text{km}^{-1}$), (b) differential reflectivity (dB), (c) rainwater content (g m^{-3}), and (d) precipitation ice water content (g m^{-3}) at 2040 UTC 24 May. Bin size is 0.25 units for all variables.

ary condition. Therefore, only the CFAD and mean profile of horizontal winds and the divergence field, which are less sensitive to the boundary conditions, are shown. Not surprisingly, the maximum of mean convergence peaked at the lowest level. The magnitude of the convergence decreased gradually until 4 km MSL. Weak convergence existed up to 8 km MSL. This deep layer of convergence implied an elevated maximum vertical velocity at that time.

To compliment the statistical kinematic properties of the squall line above, we present the mean profiles and CFAD diagrams of the specific differential phase, differential reflectivity, rainwater content, and precipitation ice water content at 2040 UTC in Fig. 11. On 24 May 1998, the mean K_{DP} near the surface was approximately $0.7^{\circ} \text{km}^{-1}$ (Fig. 11a), corresponding to a rain rate (R) of 24 mm h^{-1} (Table 1). This relatively large value of mean rain rate is consistent with a large fraction of convective rainfall and a relatively small area of light, stratiform rain compared to other tropical regimes. The highest frequency ($>30\%$) of occurrence of K_{DP} near the surface was $0.25^{\circ} \text{km}^{-1}$ or about 10 mm h^{-1} , again confirming the limited amount of stratiform echo. The 1% frequency line near the surface for K_{DP}

(R) was about $2.6^{\circ} \text{km}^{-1}$ (73 mm h^{-1}). This result is close to that found in rainfall during the westerly regime with more maritime characteristics, which was characterized by a 1% line of about 80 mm h^{-1} , during TRMM-LBA (Carey et al. 2001). On the other hand, the easterly regime during TRMM-LBA with more continental characteristics was characterized by a 1% line of about 100 mm h^{-1} . As expected, the largest values of Z_{DR} occurred well below the height of the 0°C level associated with big raindrops (Fig. 11b). The mean Z_{DR} (D_m) for raindrops near the surface was about 0.5 dB (1.2 mm). The (1%, 0.1%) occurrence line for Z_{DR} and D_m was (1.6 and 2.2 dB) and (2.0 and 2.4 mm), respectively. Comparable values for (1%, 0.1%) occurrence during the easterly and westerly regime of TRMM-LBA were (2.1 and 3.0 mm) and (1.9 and 2.5 mm), respectively (Carey et al. 2001).

Of course, precipitation ice and rainwater occurred primarily above and below the melt level at about 5 km MSL, respectively (Figs. 11c,d). Most precipitation rain and ice water contents were below about 0.5 and 0.3 g m^{-3} , respectively. Note that the anomalies in precipitation content near 5 km are associated with the inability of the polarimetric method to differentiate small

raindrops (<1 mm) from precipitation ice. As a result, it is not possible to detect with confidence very low rain (ice) contents above (below) the height of the 0°C level. The mean and maximum rainwater contents increased with distance below the melt level. Maximum rainwater contents for this case approached 5 g m^{-3} . Comparable values during the easterly (westerly) regime over the Amazon during TRMM-LBA were 10 g m^{-3} (6 g m^{-3}) (Carey et al. 2001; Cifelli et al. 2002). The largest ice water contents ($0.5\text{--}2\text{ g m}^{-3}$) occurred in the mixed-phase zone between 5 and 8 km. Similar maximum ice water contents occurred in the westerly regime over the Amazon during TRMM-LBA (Cifelli et al. 2002). On the other hand, maximum ice water contents in the easterly regime over the Amazon were typically from 3 to 8 g m^{-3} in the mixed-phase zone. Consistent with the reflectivity CFADs above, the frequency of ice water contents in excess of 1 g m^{-3} for this case decreased rapidly from 5 to 8 km.

Overall, we found that precipitation characteristics inferred from polarimetric radar for this case over the SCS during SCSMEX were similar to the westerly regime over the southwestern Amazon during TRMM-LBA. Both of them had lower rain rates and rainwater contents, smaller raindrops, and significantly lower ice water contents between 5 and 8 km than the precipitation over the Amazon during the easterly regime of the TRMM-LBA.

8. Summary

In this study, dual-Doppler and polarimetric radar analyses were combined for the first time to study the structure and rainfall characteristics of an oceanic squall-line system. Our focus was to link the kinematics of the convective system to the microphysical fields. The similarities and differences of this squall-line system occurring in the late SCS summer monsoon onset with tropical and subtropical squall lines observed in previous studies were also discussed.

On 24 May 1998, the onset of the SCS summer monsoon was near its completion with the establishment of the southwesterly flow at low levels and northeasterly winds at upper levels over the SCS region. Compared to the tropical and subtropical oceanic squall lines documented in the literature, the squall lines studied here had significant departures from the archetypal conceptual model. Characterized by convection with maximum radar reflectivity about 55 dBZ, the squall lines had little stratiform precipitation. The stratiform rain coverage accounted for only 10%–15% of total rain area, compared to an overall 63%–70% of stratiform occurrence during four TRMM field experiments in the Tropics. The dominance of convective echo was likely related to the environmental conditions, that is,

the dry air aloft along with the weak system-relative upper-level winds. For the oceanic squall-line case studied herein, the weak vertical velocity and limited buoyancy were not able to generate a strong enough mesoscale circulation to overcome the deleterious microphysical effects of evaporation in a dry environment or further form a large area of stratiform rain. The moistening of the midlevel shown in the sounding taken after the passage of the first squall line confirmed the quick evaporation of hydrometers carried aloft by weak updraft. Meanwhile, the weak environmental winds at the upper level also limited the extension of the possible stratiform rain by failing to advect the hydrometers away from the convective part. From a vertical cross section, we were able to catch a limited formation of stratiform rain associated with an intense cell from the second squall line. Different from the typical position of the stratiform rain that is usually behind its convective counterpart, the stratiform rain observed here was ahead of the convective core. It is believed that the relative weak vertical circulation observed in this study could not produce a strong cold pool sufficient to produce an upshear-tilted (trailing stratiform) convection. In addition, a pronounced low-level jet, often observed in tropical squall lines, was missing in this case. The absence of the low-level jet removed the reverse shear above the jet and prevented the development of trailing stratiform rain. This type of leading-stratiform mode, although much less frequently observed than trailing-stratiform mode before, occurred quite often during the onset period of SCS summer monsoon.

Differences in the kinematic structure of the squall lines in this study compared to other tropical and subtropical squall lines documented in previous studies may play an important role in deciding the mode of stratiform precipitation. In a typical tropical oceanic squall line, strong low-level convergence and updrafts are found in a narrow zone close to the leading edge where the inflow interacts with the cold pool resulting from evaporation cooling. The new cells form ahead of the old ones. The low-level updrafts then go upward to the rear portion of the system and form stratiform rain there. A large area of downdrafts is often observed behind the convective core. However, for the case of 24 May, the low-level convergence and updrafts were located in a wider convective area in the rear portion of the system. The new cells formed behind the old ones, and the updrafts turned forward like a return flow at the mid- to upper levels, bringing hydrometers ahead of the convective core. Weak downdrafts ahead of the updrafts were also evident. In addition to the many differences of the squall lines observed on 24 May from previously studied tropical and subtropical oceanic

squall lines, some similarities between them are also noteworthy: 1) the low-level inflow from the air ahead of the leading edge, 2) the maximum radar reflectivity at the lowest levels, 3) the gradual decrease of mean reflectivity with height below the melting layer and above 8 km MSL, and 4) the strong mean reflectivity gradient from the 0°C isotherm level to 8 km MSL implying a relatively weak updraft.

The rain and hydrometeor characteristics of the squall line were also examined. The height and magnitude of the differential reflectivity were low compared to the other analyses on tropical MCS. During the early stage of the SCS summer monsoon, the low-level convergence and updrafts were relatively weak and unable to lift the hydrometers to a higher level. In developing cells, the gentle low-level updrafts allowed sufficient time for the collision-coalescence process to develop both large raindrops and high rainwater contents. However the weak low-level updrafts were unable to lift the largest raindrops found at the lowest level farther upward. Those large drops were offset below the maximum water content due to size sorting by the updraft. There was no indication of the lofting of raindrops above the freezing level due to weak updrafts in the midlevels. As a result, there is very little precipitation ice mass in the cell. In the mature cell, the maximum rainwater content was collocated with the maximum Z_{DR} at the lowest level as the large raindrops had already precipitated out because of the weak updrafts. Midlevel updrafts were larger in the mature phase as compared to the developing convection and were capable of lofting a small zone of supercooled raindrops about 1 km above the freezing level. However, the vertical extent of the Z_{DR} column (Figs. 7d, 10) was modest and hence supercooled drops and enhanced precipitation ice mass associated with frozen drops were present only in the lowest (or warmest) portions of the mixed-phase zone.

From a statistical point of view, compared to the studies focusing on tropical convection observed during the TRMM-LBA experiment, we found that precipitation characteristics of this case over the SCS monsoon region during SCSMEX were similar to the westerly regime over the Amazon monsoon region during TRMM-LBA. However, higher rain rates and rainwater contents, larger raindrops, and significantly higher ice water contents between 5 and 8 km defined the precipitation over the Amazon during the easterly regime of the TRMM-LBA.

Acknowledgments. The authors would like to acknowledge those who participated in SCSMEX, especially Thomas Rickenbach (NASA GSFC), Robert Cifelli (Colorado State University), Paul Kucera (Uni-

versity of Iowa), Tom Keenan (BMRC, Australia), and John Gerlach (NASA WSFC) for their involvement in the radar observations and preliminary data processing. Thanks also go to Drs. Robert Adler, W.-K. Tao (NASA GSFC), and Profs. Richard Johnson and Steve Rutledge (Colorado State University) for many stimulating discussions about the MCS associated with monsoon circulation. The constructive suggestions by two anonymous reviewers also improved the presentation of this study. This research was sponsored by NASA under TRMM Grant NAG5-9699.

REFERENCES

- Atlas, D., and C. W. Ulbrich, 2000: An observationally based conceptual model of warm oceanic convective rain in the Tropics. *J. Appl. Meteor.*, **39**, 2165–2181.
- Barnes, G. M., and K. Sieckman, 1984: The environment of fast- and slow-moving tropical mesoscale convective cloud lines. *Mon. Wea. Rev.*, **112**, 1782–1794.
- Biggerstaff, M. I., and R. A. Houze Jr., 1991: Kinematic and precipitation structure of the 10–11 June 1985 squall line. *Mon. Wea. Rev.*, **119**, 3035–3065.
- Bringi, V. N., and V. Chandrasekar, 2001: *Polarimetric Doppler Weather Radar: Principles and Applications*. Cambridge University Press, 636 pp.
- Carey, L. D., and S. A. Rutledge, 2000: The relationship between precipitation and lightning in tropical island convection: A C-band polarimetric radar study. *Mon. Wea. Rev.*, **128**, 2687–2710.
- , R. Cifelli, W. A. Peterson, S. A. Rutledge, and M. A. F. Silva Dias, 2001: Characteristics of Amazonian rain measured during TRMM-LBA. Preprints, *30th Int. Conf. on Radar Meteorology*, Munich, Germany, Amer. Meteor. Soc., 682–684.
- Chong, M., P. Amayenc, G. Scialom, and J. Testud, 1987: A tropical squall line observed during the COPT 81 experiment in West Africa. Part I: Kinematic structure inferred from dual-Doppler radar data. *Mon. Wea. Rev.*, **115**, 670–694.
- Cifelli, R., C. R. Williams, D. K. Rajopadhyaya, S. K. Avery, K. S. Gage, and P. T. May, 2000: Drop-size distribution characteristics in tropical mesoscale convective systems. *J. Appl. Meteor.*, **39**, 760–777.
- , W. A. Peterson, L. D. Carey, and S. A. Rutledge, 2002: Radar observation of the kinematic, microphysical, and precipitation characteristics of two MCSs in TRMM-LBA. *J. Geophys. Res.*, **107**, 8077, doi:10.1029/2000JD000264.
- Cotton, W. R., and R. A. Anthes, 1989: *Storm and Cloud Dynamics*. Academic Press, 883 pp.
- Davies-Jones, R. P., 1979: Dual-Doppler radar coverage area as a function of measurement accuracy and spatial resolution. *J. Appl. Meteor.*, **18**, 1229–1233.
- DeMott, C. A., and S. A. Rutledge, 1998: The vertical structure of TOGA COARE convection. Part I: Radar echo distributions. *J. Atmos. Sci.*, **55**, 2730–2747.
- Ding, Y., and Y. Liu, 2001: Onset and the evolution of the summer monsoon over the South China Sea during SCSMEX field experiment in 1998. *J. Meteor. Soc. Japan*, **79**, 255–276.
- Doviak, R. J., and D. S. Zrnic, 1993: *Doppler Radar and Weather Observations*. Academic Press, 562 pp.
- Fovell, R. G., and Y. Ogura, 1988: Numerical simulation of a midlatitude squall line in two dimensions. *J. Atmos. Sci.*, **45**, 3846–3879.
- , and —, 1989: Effect of vertical wind shear on numerically

- simulated multicell storm structure. *J. Atmos. Sci.*, **46**, 3144–3176.
- Golestani, Y., V. Chandrasekar, and V. N. Bringi, 1989: Intercomparison of multiparameter radar measurements. Preprints, *24th Conf. on Radar Meteorology*, Tallahassee, FL, Amer. Meteor. Soc., 309–314.
- Gray, W. M., and R. W. Jacobson, 1977: Diurnal variation of deep cumulus convection. *Mon. Wea. Rev.*, **105**, 1171–1188.
- Halverson, J. B., T. Rickenbach, B. Roy, H. Pierce, and E. Williams, 2002: Environmental characteristics of convective systems during TRMM-LBA. *Mon. Wea. Rev.*, **130**, 1493–1509.
- Houze, R. A., Jr., 1977: Structure and dynamics of a tropical squall-line system. *Mon. Wea. Rev.*, **105**, 1540–1567.
- , 1993: *Cloud Dynamics*. Academic Press, 573 pp.
- Johnson, R. H., and P. E. Ciesielski, 2002: Characteristics of the 1998 summer monsoon onset over the northern South China Sea. *J. Meteor. Soc. Japan*, **80**, 561–578.
- Jorgensen, D. P., and M. A. LeMone, 1989: Vertical velocity characteristics of oceanic convection. *J. Atmos. Sci.*, **46**, 621–640.
- , —, and B. J.-D. Jou, 1991: Precipitation and kinematic structure of an oceanic mesoscale convective system. Part I: Convective line structure. *Mon. Wea. Rev.*, **119**, 2608–2637.
- , —, and S. B. Trier, 1997: Structure and evolution of the 22 February 1993 TOGA COARE squall line: Aircraft observations of precipitation, circulation, and surface energy fluxes. *J. Atmos. Sci.*, **54**, 1961–1985.
- Keenan, T. D., and R. E. Carbone, 1992: A preliminary morphology of precipitation systems in tropical northern Australia. *Quart. J. Roy. Meteor. Soc.*, **118**, 283–326.
- , and S. A. Rutledge, 1993: Mesoscale characteristics of monsoonal convection and associated stratiform precipitation. *Mon. Wea. Rev.*, **121**, 352–374.
- , N. Zhao, F. Lei, V. Bringi, J. Nystuen, and M. Whimpey, 2001: A comparison of radar rainfall estimators during the South China Sea Monsoon Experiment (SCSMEX). Preprints, *30th Int. Conf. on Radar Meteorology*, Munich, Germany, Amer. Meteor. Soc., 603–607.
- Lau, K.-M., and Coauthors, 2000: Report of the field operations and early results of the South China Sea Monsoon Experiment (SCSMEX). *Bull. Amer. Meteor. Soc.*, **81**, 1261–1270.
- , X. Li, and H.-T. Wu, 2002: Evolution of the large scale circulation, cloud structure and regional water cycle associated with the South China Sea monsoon during May–June, 1998. *J. Meteor. Soc. Japan*, **80**, 1129–1147.
- Leise, J. A., 1981: A multidimensional scale-telescoped filter and data extension package. NOAA Tech. Memo. ERL WPL-82, 18 pp.
- LeMone, M. A., G. M. Barnes, E. J. Szoke, and E. J. Zipser, 1984: The tilt of the leading edge of mesoscale tropical convective lines. *Mon. Wea. Rev.*, **112**, 510–519.
- , E. J. Zipser, and S. B. Trier, 1998: The role of environmental shear and thermodynamic conditions in determining the structure and evolution of mesoscale convective systems during TOGA COARE. *J. Atmos. Sci.*, **55**, 3493–3518.
- Lewis, S. A., M. A. LeMone, and D. P. Jorgensen, 1998: Evolution and dynamics of a late-stage squall line that occurred on 20 February 1993 during TOGA COARE. *Mon. Wea. Rev.*, **126**, 3189–3212.
- Mohr, C. G., L. J. Miller, R. L. Vaughan, and H. W. Frank, 1986: The merger of mesoscale datasets into a common Cartesian format for efficient and systematic analyses. *J. Atmos. Oceanic Technol.*, **3**, 143–161.
- Parker, M. D., 2002: Dynamics of convective lines with leading precipitation. Preprints, *21st Conf. on Severe Local Storms*, San Antonio, TX, Amer. Meteor. Soc., 5–8.
- , and R. H. Johnson, 2000: Organizational modes of midlatitude mesoscale convective systems. *Mon. Wea. Rev.*, **128**, 3413–3436.
- Raymond, D. J., 1994: Convective processes and tropical atmospheric circulations. *Quart. J. Roy. Meteor. Soc.*, **120**, 1431–1455.
- Robe, F. R., and K. A. Emmanuel, 2001: The effect of vertical wind shear on radiative–convective equilibrium states. *J. Atmos. Sci.*, **58**, 1427–1445.
- Rotunno, R., J. B. Klemp, and M. L. Weisman, 1988: A theory for strong, long-lived squall lines. *J. Atmos. Sci.*, **45**, 463–485.
- Roux, F., 1988: The West African squall line observed on 23 June 1981 during COPT 81: Kinematics and thermodynamics of the convective region. *J. Atmos. Sci.*, **45**, 406–426.
- Simpson, J., Ed., 1988: TRMM: A satellite mission to measure tropical rainfall. Science Steering Group Rep., National Aeronautics and Space Administration, Goddard Space Flight Center, Greenbelt, MD, 94 pp.
- Steiner, M., R. A. Houze Jr., and S. E. Yuter, 1995: Climatological characteristics of three-dimensional storm structure from operational radar and rain gauge data. *J. Appl. Meteor.*, **34**, 1978–2007.
- Tao, S., and L. Chen, 1987: A review of recent research on the East Asian summer monsoon in China. *Monsoon Meteorology*, C.-P. Chang and T. N. Krishnamurti, Eds., Oxford University Press, 60–92.
- Tao, W.-K., and J. Simpson, 1989: Modeling study of a tropical squall-type convective line. *J. Atmos. Sci.*, **46**, 177–202.
- , C.-L. Shie, J. Simpson, S. Braun, R. H. Johnson, and P. E. Ciesielski, 2003: Convective systems over the South China Sea: Cloud-resolving model simulations. *J. Atmos. Sci.*, **60**, 2929–2956.
- Tokay, A., and Coauthors, 2001: On the role of drop size distribution in TRMM rain profiling algorithm. Preprints, *30th Int. Conf. on Radar Meteorology*, Munich, Germany, Amer. Meteor. Soc., 345–347.
- Trier, S. B., W. C. Skamarock, M. A. LeMone, D. B. Parsons, and D. P. Jorgensen, 1996: Structure and evolution of the 22 February 1993 TOGA COARE squall line: Numerical simulations. *J. Atmos. Sci.*, **53**, 2861–2886.
- , —, and —, 1997: Structure and evolution of the 22 February 1993 TOGA COARE squall line: Organization mechanisms inferred from numerical simulation. *J. Atmos. Sci.*, **54**, 386–407.
- Wang, J.-J., 2004: Evolution and structure of the mesoscale convection and its environment: A case study during the early onset of the southeast Asian summer monsoon. *Mon. Wea. Rev.*, **132**, 1104–1120.
- Wang, T.-C. C., Y.-J. Lin, R. W. Pasken, and H. Shen, 1990: Characteristics of a subtropical squall line determined from TAMEX dual-Doppler data. Part I: Kinematic structure. *J. Atmos. Sci.*, **47**, 2357–2381.
- Yuter, S. E., and R. A. Houze Jr., 1995: Three-dimensional kinematic and microphysical evolution of Florida cumulonimbus. Part II: Frequency distributions of vertical velocity, reflectivity, and differential reflectivity. *Mon. Wea. Rev.*, **123**, 1941–1963.
- Zipser, E. J., 1969: The role of organized unsaturated convective downdrafts in the structure and rapid decay of an equatorial disturbance. *J. Appl. Meteor.*, **8**, 799–814.
- , 1977: Mesoscale and convective-scale downdrafts as distinct components of squall-line structure. *Mon. Wea. Rev.*, **105**, 1568–1589.
- , and M. A. LeMone, 1980: Cumulonimbus vertical velocity events in GATE. Part II: Synthesis and model core structure. *J. Atmos. Sci.*, **37**, 2458–2469.
- , and K. Lutz, 1994: The vertical profile of radar reflectivity of convective cells: A strong indicator of storm intensity and lightning probability? *Mon. Wea. Rev.*, **122**, 1751–1759.